ISSN (Print) 1226-1750
ISSN (Online) 2233-6656
Journal of Magnetics 28(4), 361-373 (2023) https://doi.org/10.4283/JMAG.2023.28.4.361

Characteristics Analysis and Optimization of Secondary Permanent Magnet Flux-Switching Linear Machines

Haichao Feng*, Yaohua Guo, Xiaozhuo Xu, Caixia Gao, and Liwang Ai

School of Electrical Engineering and Automation, Henan Polytechnic University, Jiaozuo 454000, China

(Received 5 February 2023, Received in final form 27 September 2023, Accepted 27 September 2023)

In order to meet the demand of high-power density, high-precision positioning and low cost direct drive system in ropeless lifting, precision machining and other fields, the modular secondary structure with permanent magnet synchronous magnetization is adopted in this paper, and the secondary permanent magnet flux-switching linear machine (SPMFSLM) is proposed. Compared with the traditional primary permanent magnet flux-switching linear machine (PPMFSLM), it reduces the thrust ripple and strengthens the primary structure. According to the topology and operation principle of the machine, starting from the air-gap magnetic field modulation principle and the convex tooth effect, the contribution of the air-gap flux density harmonics of the permanent magnet magnetic field and the armature magnetic field for the two machines to the average thrust is compared and analyzed, reflecting the similarities and differences between the two FSLMs in the thrust generation mechanism. In addition, the no-load characteristics for back-EMF and the thrust characteristics for two machines under equal load are calculated and compared. Finally, the multi-objective optimization of the key structural parameters of the machine is carried out by combining the response surface method (RSM) with the NSGAII algorithm. Then, the 3D simulation of the machine was carried out and cross-validated with the 2D results. Finally, a double-sided SPMFSLM (DS-SPMFSLM) is proposed from the practical point of view. The performance of DS-SPMFSLM is significantly superior to that of single-sided SPMFSLM, which verifies the advantages of the secondary permanent magnet structure scheme.

Keywords : flux-switching, linear machine, magnetic field modulation, response surface method, NSGAII, DS-SPMFSLM

1. Introduction

In recent years, the permanent magnet linear machine has attracted numerous scholars to study it deeply, due to its simple structure, fast response, as well as high precision [1, 2]. In ropeless lifting, precision machining, large-scale mining, and other areas of demand for high thrust, direct drive, and high-precision positioning, it has great potential applications [3-5]. Despite the fact that thrust quality is the key to high dynamic response and high positioning accuracy of permanent magnet linear machines, it is equally significant to increase thrust and decrease operating fluctuations while minimizing manufacturing costs. Based on this, several permanent magnet flux-switching linear machines with high efficiency, high fault tolerance, and a broad speed range are proposed [6]. According to the different positions of permanent magnet, primary and secondary permanent magnet structures can be distinguished.

Besides, the traditional primary permanent magnet flux-switching linear machine (PPMFSLM) usually adopts an N-S alternating PM array, which has large thrust fluctuation and serious magnetic saturation of primary teeth. Moreover, the researchers have effectively suppressed the thrust fluctuation of the machine by slotting the primary teeth [7], adding the modulation teeth [8], as well as the primary modular scheme [9]. A dual-stator flux-switching linear machine is proposed in Reference [11] due to the dual-stator structure's effectiveness in enhancing the power factor and thrust density of the machine [10], and the permanent magnet and armature are placed on both sides of the mover, with high thrust density and power factor. Additionally, the multi-tooth, yokeless, hybrid excitation and segmented design are applied to the double-sided structure, and the proposed integrated topology enhances the electromagnetic performance [12-17].

©The Korean Magnetics Society. All rights reserved.
*Corresponding author: Tel: +86-13462847991
Fax: +86-0391-3987552, e-mail: fhc@hpu.edu.cn

© 2023 Journal of Magnetics

In view of the above research status, this paper introduces a longitudinal flux structure, which is a modular secondary permanent magnet flux-switching linear machine. Moreover, the PM magnetized in the same direction and the silicon steel sheets on both sides together constitute a unit. In comparison to the traditional FSLM, there is a significant reduction in PM consumption, a further enhancement in thrust density, and a reduction in thrust ripple due to the increased number of secondary teeth, leading to an increase in the harmonic frequency.

When optimizing the machine, the traditional optimization method can only consider the impact of a single factor almost every time, and the low fluctuation is frequently accompanied by the cost of the average thrust sacrifice. Furthermore, multi-objective optimization problems (MOPs) provide a set of trade-off solutions, the Pareto solution set [18, 19], which can maximize multiple objectives concurrently and assigning different weights to each objective. Currently, the combination of the response surface method (RSM) and stochastic evolutionary algorithm has been employed in machine optimization [20], which considerably reduces the computational cost and optimization time.

In this paper, the similarities and differences between the SPMFSLM and PPMFSLM topologies and electromagnetic thrust generation mechanisms are compared and analyzed from two perspectives: the air-gap magnetic field modulation principle and the convex tooth effect. In the third section, the no-load characteristics including back-EMF, and the load characteristics such as thrust are calculated and compared. In the fourth section, based on the sensitivity analysis of the key parameters of the machine, the multi-objective optimization is performed by combining the response surface method (RSM) with the NSGAII algorithm, and the resulting parameter combination is used for modeling. Similarly, the performance of the machine prior to and after optimization is compared and analyzed and the effectiveness of the multi-objective optimization method is verified. Finally, the consistency between theoretical analysis and simulation results serves as validation for the accuracy and efficacy of the proposed scheme.

2. Topology and Operation Principle

2.1. Topology

The traditional PPMFSLM topology is demonstrated in Fig. 1(a). Besides, the primary is assembled by alternating magnetized permanent magnets at adjacent positions and a U-shaped core, which the armature windings are wound on. Furthermore, the coexistence of PM and armature windings on the primary side constitutes a spatial competition relationship, which reduces the space available for armature windings and iron laminations. Subsequently, the further improvement of the electromechanical load is constrained, which ultimately affects the increase of the thrust density of the machine. Additionally, there are issues such as a significant thrust ripple and magnetic saturation in the primary teeth.

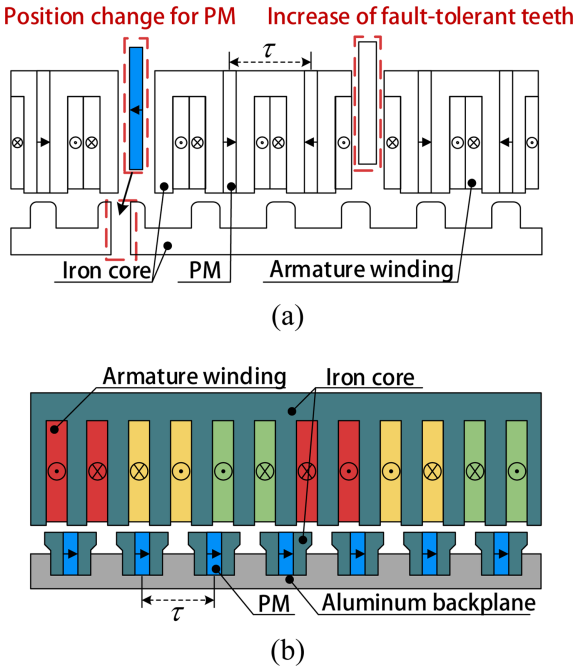

Fig. 1. (Color online) SPMFSLM structure evolution. (a) PPMFSLM, (b) SPMFSLM.

The SPMFSLM topology is illustrated in Fig. 1. Furthermore, the PM position of the PPMFSLM is moved from the primary to the middle of the secondary teeth, and the bottom support plate is made of non-magnetic material. In the meantime, fault-tolerant teeth are added between the primary coils to make distinct permanent magnet magnetic circuits independent of each other. The armature winding follows a centralized winding structure and is wound on the primary core teeth to constitute the primary machine. The secondary section consists of 7 module units, all securely positioned within a groove of the non-magnetically conductive component. Each module unit is composed of a permanent magnet and convex teeth on both sides. Among them, all PMs have the same magnetization direction and distinct PM unit modules are isolated by non-magnetic materials to avoid short circuits. Additionally, the increase in fault-tolerant teeth improves the fault-tolerant ability of the machine during operation. Simultaneously, the coil winding end's length is further minimized, leading to a reduction in copper loss, de-

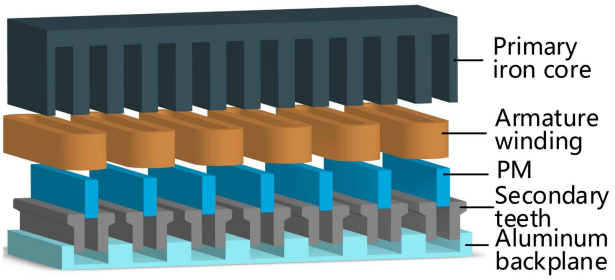

Fig. 2. (Color online) SPMFSLM three-dimensional structure diagram.

creased end leakage inductance, and enhanced machine efficiency. The three-dimensional configuration of the machine is depicted in Fig. 2.

2.2. Operation Principle Analysis

The operation process of the SPMFSLM is revealed in Fig. 3. With a shift in relative position, the flux linkage path shifts, resulting in a shift in PM flux distribution. Fig. 3 serves as the PM flux distribution diagram of the primary part of the machine and the secondary module unit in four special positions. Under the condition where the initial position corresponds to Fig. 3(a), the secondary tooth R1 aligns with the primary tooth A1, permitting the entry of PM flux linkage into the primary tooth via the air-gap from the secondary tooth. This formation results in a winding flux linkage, during which the PM flux linkage reaches its maximum amplitude. As it transitions to the position in Fig. 3(b), the PM aligns with the primary teeth, causing the magnetic flux generated by the armature winding to become 0. Upon further advancement of the machine to the position shown in Fig. 3(c), the secondary tooth R2 of the SPMFSLM aligns with the primary tooth A1, instigating a transformation in the flux path. The PM flux linkage passes through the secondary tooth R1 through the air gap into the primary tooth, forming the winding flux linkage. Currently, in reverse, the flux linkage flux in the coil is greatest. When in the position in Fig. 3(d), the permanent magnet located in the secondary module unit is opposite to the primary tooth, and the magnetic flux formed in the coil is 0. It is evident from this that with the continuous change of the relative position between the primary and secondary mechanical secondary, the continuous switching of the path of the PM flux linkage through the winding leads to alterations in the magnetic flux within the coil, consequently generating a sinusoidal distribution of the induced potential. When a set of three-phase sinusoidal currents with the same phase are introduced, subsequently, a stable electromagnetic thrust can be generated to drive the machine forward.

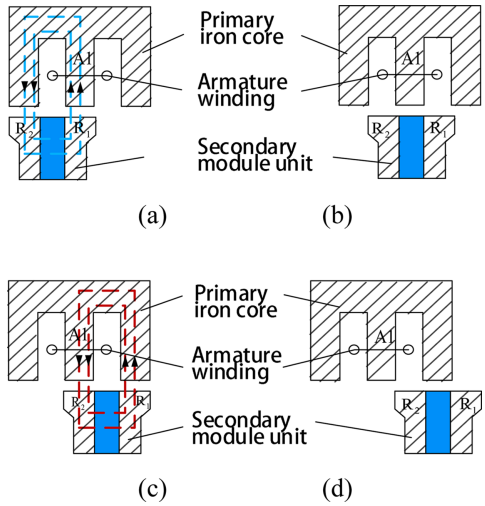

Fig. 3. (Color online) Open-circuit flux distributions of coil at different mover positions.

Table 1. Key structural parameters of two machines.

Specifications	Value	
	PPMFSLM	SPMFSLM
Primary teeth N_p	12	
Primary slot width w_{ps} (mm)	5.5	7.8
Number of turns per coil N_{coil}	145	
Stack length l_a (mm)	75	
Air-gap length g (mm)	2	
Secondary pole pitch τ_s (mm)	25.71	
PM width w_{pm} (mm)	4.5	5.8
PM height h_{pm} (mm)	54.4	16
Secondary teeth width w_{pt} (mm)	11	6.8
Backplane yoke length (mm)	8.9	10.1
PM dosage (cm^3)	110.16	48.72
Iron lamination type	DW470-50A	
PM type	N48H	

As indicated in Table 1, the key geometric dimensions and related parameters of the two flux-switching machines PPMFSLM and SPMFSLM are listed. To facilitate the comparison of mechanical characteristics, the current density, axial length, permanent magnet grade, as well as magnetic steel used in SPMFSLM are consistent with PPMFSLM.

3. Electromagnetic Characteristics Analysis

3.1. PM field

The magnetic flux density of the PM field of the PPMFSLM and SPMFSLM is shown in Fig. 4. The both two machines have different degrees of magnetic flux

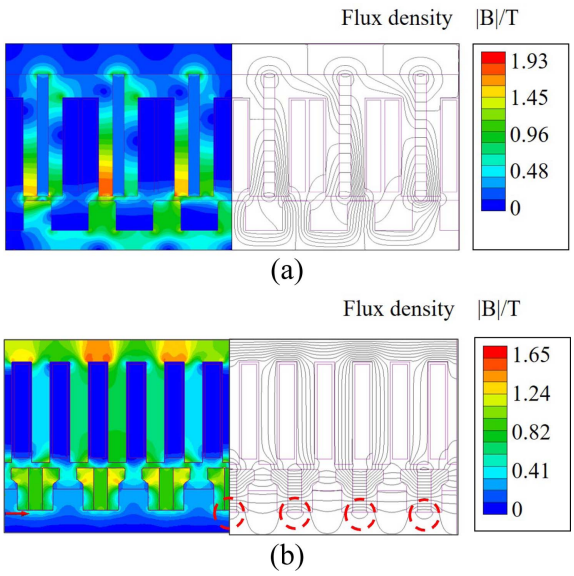

Fig. 4. (Color online) Open-circuit flux density distributions. (a) PPMFSLM. (b) SPMFSLM.

leakage at the top and bottom respectively. For PPMFSLM, the magnetic density saturation of the primary teeth is serious. On the one hand, the convex tooth structure of the secondary has a magnetic concentration effect, which has a significant effect on the improvement of air-gap flux density, but it also brings greater fluctuations, affecting the stability of machine operation; the overall magnetic density distribution of SPMFSLM is more uniform, and there is no local supersaturation, effectively increasing the upper limit of the machine magnetic load, as shown in Fig. 4(b), while the non-magnetic material between the secondary module units also effectively reduces the magnetic flux leakage.

The no-load air-gap flux density curves of PPMFSLM and SPMFSLM are shown in Fig. 5. Due to the secondary salient pole structure of PPMFSLM, the distortion rate of

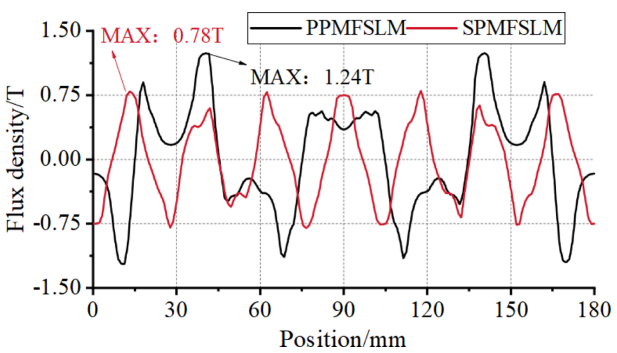

Fig. 5. (Color online) Open-circuit air-gap flux density distribution of the PPMFSLM and SPMFSLM.

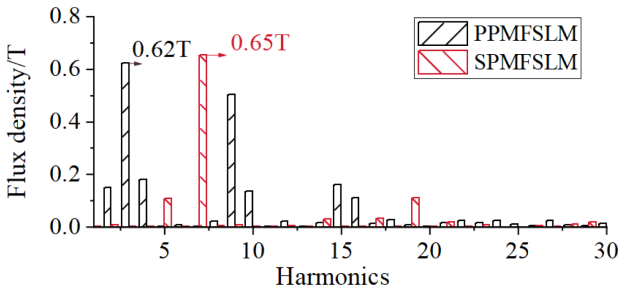

Fig. 6. (Color online) Air-gap flux density harmonic distribution of PM field for two machines.

flux density waveform is large. When the PM consumption is much higher than that of SPMFSLM, the peak flux density is 1.24 T, which is 60 % higher than the peak flux density 0.78 T of SPMFSLM. The magnetic density curve distortion rate of SPMFSLM is lower and more sinusoidal.

The results of harmonic distribution of no-load air-gap flux density of two machines based on Fourier transform analysis are shown in Fig. 6. It can be seen from the air-gap magnetic field modulation principle that in the PPMFSLM air-gap, in addition to the 3rd, 9th and 15th harmonics generated directly by the permanent magnet magnetomotive force ($(2n-1)N_{PM}$, n = 2, 5, 8), the 2nd, 4th, 10th and 16th harmonic components generated by the modulation of the primary armature teeth ($|(2n-1)N_{PM} \pm N_p|$, n = 1, k = 2 and n = 2, k = 2) are also included. For SPMFSLM, the main flux density harmonics in the air-gap are 5th, 7th and 19th. The 7th harmonic is directly generated by the magnetomotive force of the secondary permanent magnet (nN_{PM}, n = 1), while the 5th and 19th harmonics ($|nN_{PM} \pm kN_P|$, n = 1, k = 1) are generated by the modulation of the primary teeth on the permanent magnet magnetomotive force in the air-gap. Like PPMFSLM, due to the consistency and complementarity of the windings, the even harmonics in the permanent magnet

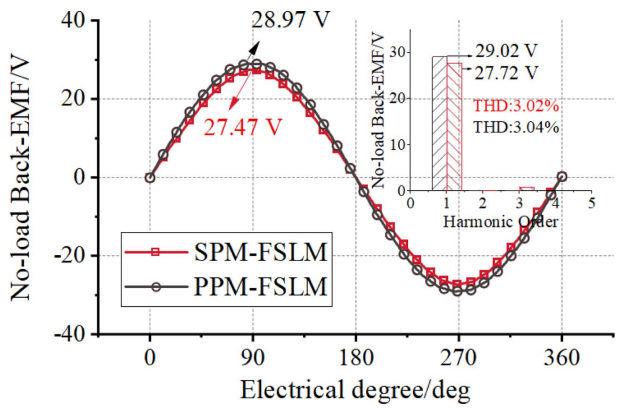

Fig. 7. (Color online) No-load back-EMF waveforms and Harmonic distributions of two flux-switching machines @ 1 m/s.

flux linkage and the induced electromotive force in the coil will be offset, thereby increasing the sinusoidality of the induced electromotive force.

The no-load back-EMF waveform and further harmonic distribution of the two machines running at 1 m/s are compared as shown in Fig. 7. Under different magnetic pole structures, the back-EMF waveforms are relatively sinusoidal. Since the amplitude of the air-gap magnetic flux density of SPMFSLM is slightly lower than that of PPMFSLM, the back-EMF amplitude of SPMFSLM is 27.47 V, which is slightly lower than 28.97 V of PPMFSLM. After Fourier decomposition calculation, the harmonics of each frequency are shown in the figure, and the harmonic content (THD) is 3.04 % and 3.02 %, respectively.

3.2. Armature field

After the three-phase symmetrical sinusoidal alternating current is introduced into the winding, the corresponding magnetomotive force will be generated in the armature. According to the vector distribution theory of slot potential [21], the pole pair of armature winding of SPMFS machine with 12s/7p is $N_{Pa} = N_{PM} = N_p$, it can be deduced that the magnetomotive force of armature reaction contains the harmonics of ($2i$–1) times the maximum convention (GCD) frequency of Ns and N_{pa}, namely $2i$–1(i = 1, 2, 3...), but does not contain the harmonics of triple frequency. The finite element analysis results of the harmonic distribution of the air-gap flux density of the armature reaction are shown in Fig. 8, where the 1st, 5th, 7th, 11 th and 19 th harmonics are generated by the direct action of the armature reaction magnetomotive force on the air-gap (i = 1, 3, 4, 6), while the 2nd, 6th, 8th and 9th harmonics are generated due to the modulation of the secondary salient tooth on the armature reaction magnetic field. The 2nd and 9th harmonics can be expressed as $|2i-1-kN_p|$(i = 3 or 5, p = 1); 6th, 8th can be expressed as $|2i-1 \pm kN_p|$(i = 1, p = 1).

PPMFSLM armature reaction air-gap flux density harmonics mainly include the 2nd, 3rd, 4th, 5th, 9th, 11th, 14th, 16th. The 2nd, 4th, 14th and 16th harmonics are directly generated by the armature reaction magnetomotive force. The 3rd, 5th, 9th and 11th harmonics are derived from the modulation of the secondary salient pole teeth, which can be expressed as $|kNp \pm 2i|$(k = 1, i = 1 or 2).

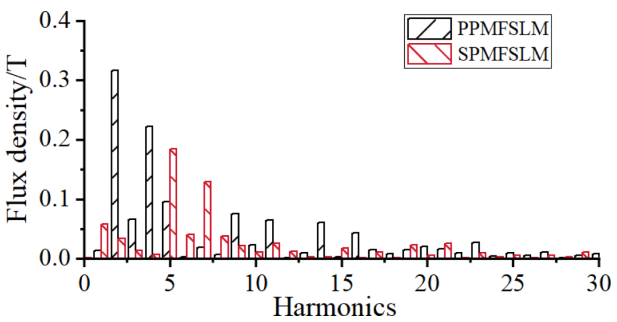

Fig. 8. (Color online) Air-gap flux density harmonic distribution of armature field for two machines.

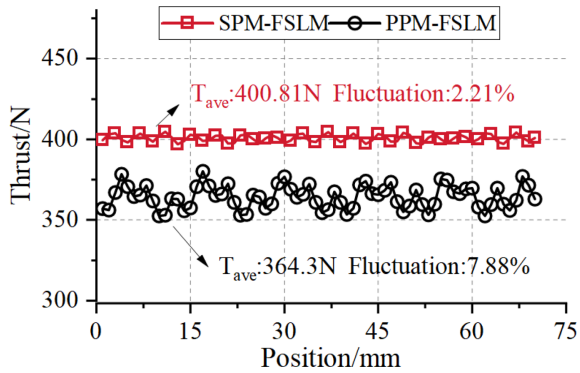

Fig. 9. (Color online) Thrust characteristics of two flux-switching machines.

3.3. Thrust characteristics

When three-phase sinusoidal alternating current with equal amplitude and frequency is introduced to the two machines, the obtained thrust waveform is shown in Fig. 9. The average thrust of PPMFSLM and SPMFSLM is 364.31 N and 400.81 N, respectively. Under the condition that the permanent magnet consumption of SPMFSLM is only 45.2 % of PPMFSLM, the permanent magnet utilization rate of SPMFSLM is 8.23 N/cm^3, which is 2.43 times of 3.38 N/cm^3 of PPMFSLM, and the thrust is 10 % higher. Under periodic boundary conditions, the thrust fluctuation of SPMFSLM is only 2.21 % lower than that of PPMFSLM 7.88 %.

In Fig. 10, the variation of mechanical thrust with current density is shown. Overall, the thrust of both

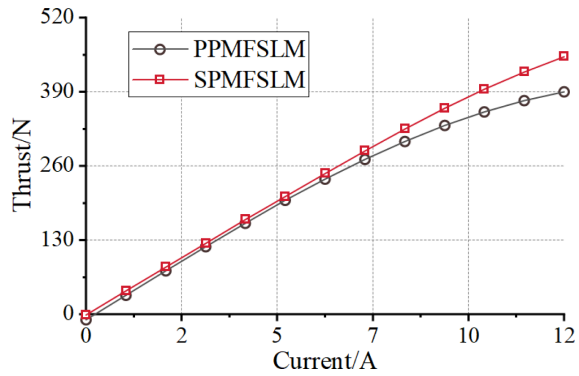

Fig. 10. (Color online) Variation diagram of thrust with current density.

machines increases with the increase of current density, but when the current exceeds 6 A, the thrust no longer has a linear relationship with the current, which is due to the gradual saturation of the magnetic circuit. Among them, the thrust reduction of PPMFSLM is more obvious. The reason is that the primary part of the armature winding gets more space to move from the primary to the secondary through the permanent magnet, so that greater thrust can be obtained at the same current density.

4. SPMFSLM Multi-objective Optimization

A multi-objective optimization method based on response surface method (RSM) and NSGAII algorithm is proposed in this paper, which has been applied to the optimization of SPMFSLM. The optimization flow chart is shown in Fig. 11, including parameter sensitivity analysis, response surface model construction and NSGAII-based algorithm optimization.

4.1. Determining optimization objectives and parameters

In order to achieve the optimal performance of SPMFSLM, the mechanical average thrust (T_{ave}), thrust ripple (T_{ripple}) and back-EMF harmonic distortion rate (THD_{emf}) are selected as the optimization objectives.

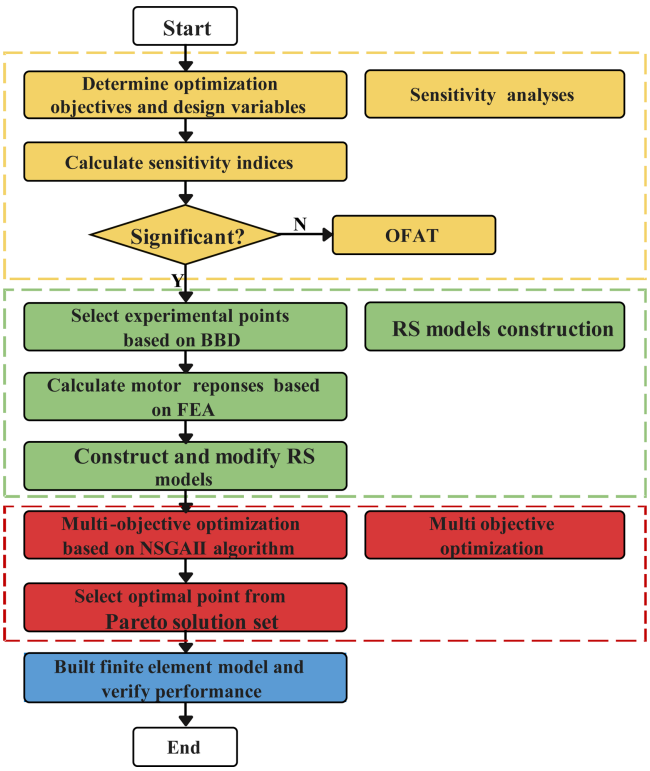

Fig. 11. (Color online) Flowchart of proposed optimization method.

Table 2. Value range of variables.

Variable	Min (mm)	Max (mm)
w_{ps} (mm)	7.8	9.4
w_{pt} (mm)	6.8	8
w_{pm} (mm)	5.4	7
h_{pm} (mm)	14.4	18

In order to further explore the influence of mechanical structure parameters on the above optimization objectives, the four structural parameters of primary side slot width, secondary tooth width, permanent magnet width and permanent magnet height are considered as optimization variables. The preliminary determination of the variation range of each structural optimization parameter is shown in Table 2.

4.2. Sensitivity analyses

In order to analyze the influence of each optimization variable on the optimization goal, sensitivity analysis is used to introduce the sensitivity index of each optimization variable :

$$\bar{S}_{ni}^{m} = \left.\frac{\partial f}{\partial z_i}\right|_{\mathrm{Nop}} \frac{z_i}{f} \simeq \frac{\Delta f / f}{\Delta z_i / z_i} \tag{1}$$

where f represents the function of design objectives and z_i is the design variables.

For the convenience of further analysis and comparison, the results of sensitivity analysis are normalized. The final results are shown in Fig. 12. The primary slot width w_{ps} has the greatest impact on THD_{emf}, and w_{pm} has a greater impact on *Thrust* and T_{ripple}.

4.3. RS models construction

The BBD(Box-Behnken Design) method was used to establish the required orthogonal test matrix. The response

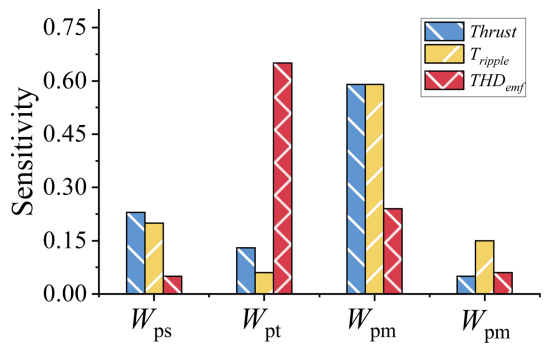

Fig. 12. (Color online) Sensitivity indices of the design variables for the three optimization objectives.

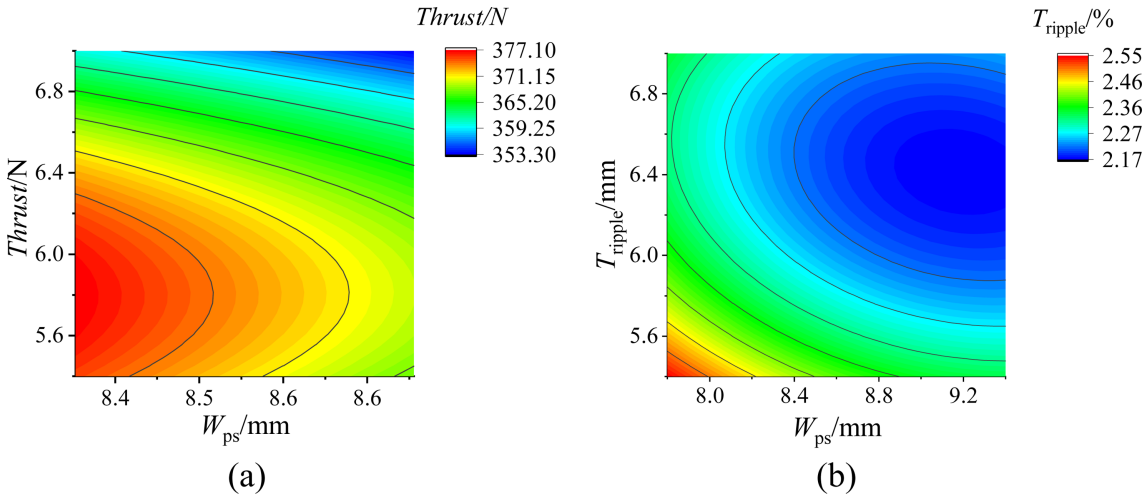

Fig. 13. (Color online) Response surface model result diagram.

values of the optimization variables at each level were obtained by finite element simulation, and then the multivariate quadratic regression equation was established by Design Expert software to fit the above-mentioned optimization target response values to obtain its mathematical model.

The second-order polynomial regression equation model can be expressed as :

$$Y = \beta_0 + \sum_{i=1}^{k} \beta_i x_i + \sum_{i=1}^{k} \beta_{ii} x_i^2 + \sum_{i,j\neq 1}^{k} \beta_{ij} x_i x_j + \varepsilon \tag{2}$$

where Y is the response variable, β_0, β_i, and β_j are regression coefficients, β_{ij} is the coefficients of product-term of two different variables and β_{jj} is coefficients of terms, which is the square of the variable itself. X_i and X_j means two different optimization variables, which means different combinations of product-term of two variables.

By considering the removal of some items with low correlation, the mathematical model is simplified. The multiple correlation coefficients R^2 of the three models were 0.996, 0.7 and 0.997, respectively, showing a high fitting degree. Fig. 13 shows the results of average thrust and thrust ripple. Through response surface analysis, it can be seen that the gradient of response surface changes obviously and the optimization parameters have the best range.

4.4. Multi objective optimization

According to the fitness function obtained by the above response surface, the NSGAII algorithm which is widely used at present is adopted. A set of Pareto solution sets is obtained by constructing a surrogate model. The flow chart of the NSGAII algorithm is shown in Fig. 14.

Weight coefficient is applied to evaluate each variable

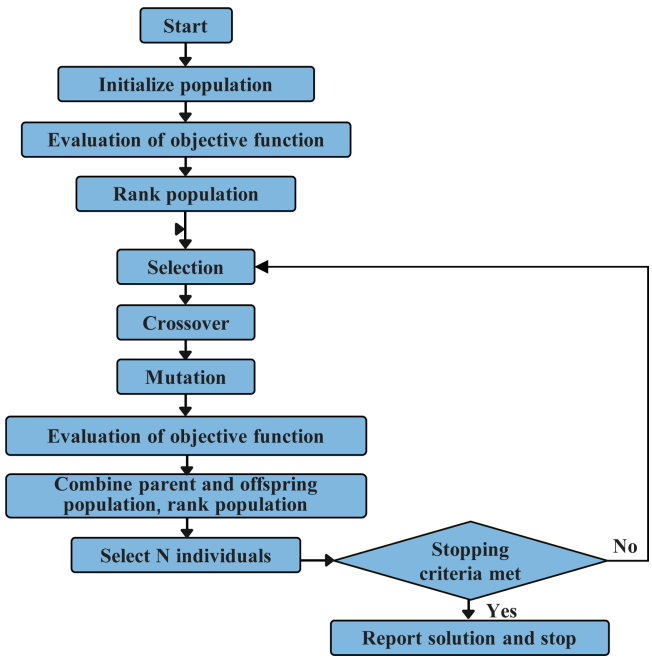

Fig. 14. (Color online) Flowchart of NSGAII.

comprehensively considering three optimization goals. A comprehensive sensitivity index $G(n_i)$ is introduced and can be described as

$$G(n_i) = w_1 \,|\, S_{Thrust} \,| + w_2 \,|\, S_{T_{ripple}} \,| + w_3 \,|\, S_{THD_{emf}} \,| \tag{3}$$

where S_{Thrust}, $S_{Tripple}$, and S_{THDemf} are the sensitivity of average thrust force, thrust ripple, and back-EMF harmonic distortion rate, respectively. Besides, w_1, w_2, and w_3 represent the weight of the average thrust force, the thrust ripple and back-EMF harmonic distortion rate, respectively, which satisfy $w_1+w_2+w_3=1$. The weight factors can be selected reasonably based on the different degrees of

demand for the optimization objectives. In the process of multi-objective optimization, the selection of weight factors is very important. However, there is no single criterion to determine the values of weight factors.

In this paper, high thrust force density is the primary pursuit for the proposed SPMFSLM machine. The stability of the operation also needs a relatively low thrust ripple. In addition, the back-EMF harmonic distortion rate as the significant advantage of the proposed machine should be considered. Hence, the value of w_1 is selected as 0.6, which is higher than the others. Also, the value of w_2 and w_3 are selected to be 0.2, which are less required.

The value range of each variable in the algorithm is shown in Table 2, and the constraint condition is that the amount of permanent magnet is constant. The initial population is set to 40, the number of iterations is 2000, and the time consumed is about 15 s, which saves a lot of time compared with the traditional finite element optimization method.

After the global optimization of the algorithm, the optimal value combination of each optimization variable is obtained as follows: primary slot width w_{ps} = 7.8 mm, secondary tooth width w_{pt} = 6.8 mm, permanent magnet width w_{pm} = 5.4 mm, permanent magnet height h_{pm} = 17.2 mm. The performance comparison before and after mechanical optimization is shown in Table 3. The average thrust of the optimized machine is 414.2 N, as shown in Fig. 15, which is increased by 3.34 %, the thrust fluctuation is reduced by 1.84 %, and the utilization rate of permanent magnet is increased by 3.65 % under the condition that the amount of permanent magnet is almost unchanged.

Table 3. Machines performance.

	Initial	Optimized
T_{avg} (N)	400.81	414.20 (↑3.34 %)
T_{ripple} (%)	2.21	2.17 (↓1.84 %)
THD_{emf} (%)	3.02	2.76 (↓9.42 %)
PM dosage (cm^3)	48.72	48.76
PM utilization (N/cm^3)	8.2	8.5 (↑3.65 %)

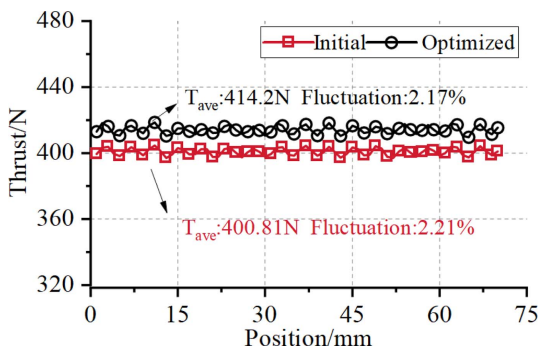

Fig. 15. (Color online) Thrust before and after optimization.

Table 4. Performance comparison between PPMFSLM and SPMFSLM.

Performance index	PPMFSLM	SPMFSLM
	FEA	FEA
Continuous thrust (N)	364.3	414.20
Velocity (m/s)	1	1
motor constant (N/√W)	73.65	76.85
Copper Loss power (W)	124.01	144.65
Output Power (W)	364.3	414.2
Pole Pitch τ (mm)	30	25.71
Continuous Current (A)	7.07	7.07
Thrust constant (N/A)	51.53	58.59
Back-EMF constant (V/m/s)	28.97	29.1

Finally, the PPMFSLM FEA model is compared with SPMFSLM. The comparison of performance indicators is shown in Table 4.

4.5. 3D simulation analysis

The 3D-SPMFSLM simulation magnetic flux density cloud diagram is shown in Fig. 16, and the overall magnetic flux density cloud diagram is shown in Fig. 16(a). The overall distribution is very uniform, and the distribution along the axial direction is more consistent. In the longitudinal direction, due to the continuous change of the relative position between the mechanical primary part and the secondary part under the condition of mechanical motion, the magnetic flux density distribution of the primary part shows obvious periodicity. In the secondary part of the machine, as shown in Fig. 16(b), it is the top view of the secondary part of the machine. The distribution law along the axial direction is that the magnetic flux density at the end is slightly higher than that in the middle, as shown in Fig. 16(b) and (c). The red circle annotation shows that a certain degree of magnetic flux leakage can be clearly observed in the lower region of the secondary part of the machine.

As shown in Fig. 17(a), the no-load back-EMF of SPMFSLM model of 2D and 3D FEA is compared. The amplitude of 2D simulation back-EMF is 28.32 V, but the maximum no-load back-EMF of 3D model is 27.47 V, which is 3.01 % lower than that of 2D model. Through harmonic analysis, the harmonic content in 2D simulation is 2.76 %, which is 92.75 % lower than that in 3D simulation (5.32 %). The reason may be that more harmonics are introduced into the no-load back-EMF of 3D simulation due to factors such as armature winding

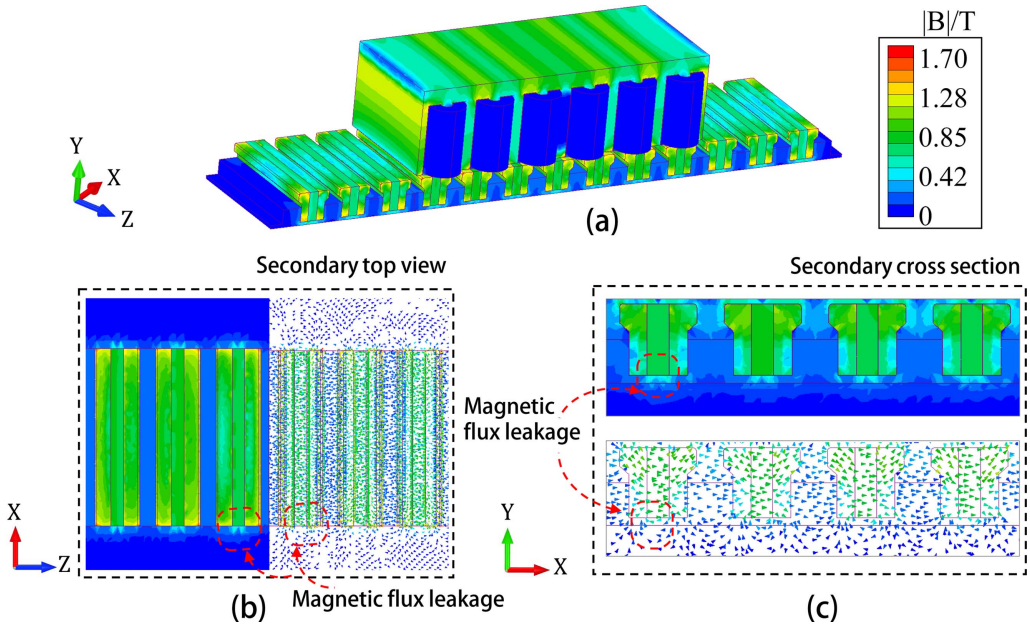

Fig. 16. (Color online) SPMFSLM three-dimensional magnetic flux density nephogram.

end and spatial electromagnetic harmonic coupling, which is closer to the actual situation. The magnetic flux leakage problem shown in Fig. 16(b) and (c) can be effectively solved by using a two-sided structure.

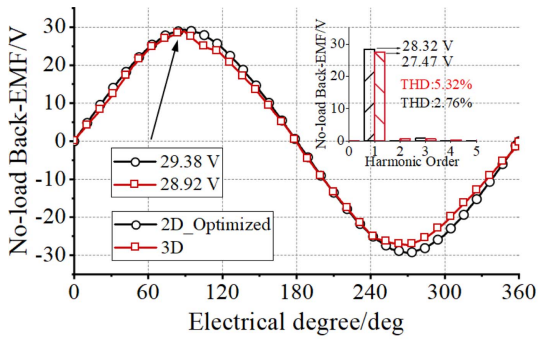

(a) No-load back-EMF

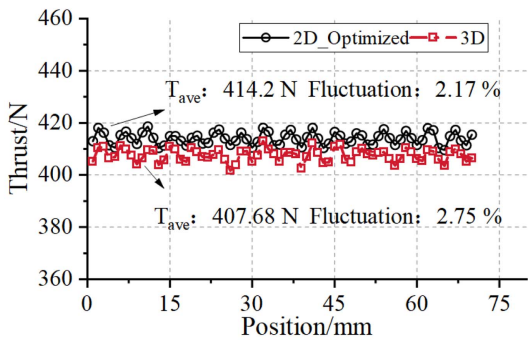

(b) Thrust characteristics

Fig. 17. (Color online) No-load back-EMF and thrust characteristics comparison between 2D and 3D FEA of SPMFSLM.

The thrust comparison of the finite element analysis of the 2D and 3D SPMFSLM models is shown in Fig. 17(b). The average thrust of the 2D model is 414.2 N, and the fluctuation is 2.17 %. The average thrust of the 3D model is 407.68 N. It can be clearly seen that the average thrust and thrust fluctuation results of 2D and 3D simulation are in good agreement, and this content has been added in the paper.

5. Practice Analysis

The practicability of SPMFSLM is analyzed in detail. At the same time, the characteristics of SPMFSLM compared with traditional PMLSM are also described. The performance comparison between PMLSM and SPMFSLM is further analyzed. Finally, an improved DS-SPMFSLM is proposed and its performance is analyzed.

Compared with the traditional PMLSM, as shown in Fig. 18(a), their working principles are different: PMLSM relies on the interaction between the armature magnetic field and the permanent magnet magnetic field, as shown in Fig. 18(b). However, SPMFSLM operates on the principle of the shortest reluctance path, as shown in Fig. 3. Their secondary structures are different. Compared with SPMFSLM, the armature winding of PMLSM is closer to the long side of the secondary permanent magnet, the coupling between the armature magnetic field and the permanent magnetic field is stronger, and the permanent magnet has a greater risk of demagnetization.

Further, the performance of SPMFSLM and PMLSM is

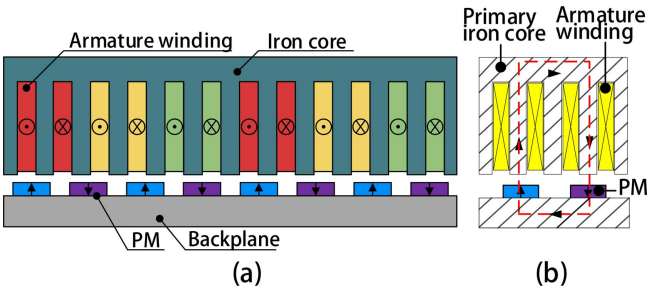

Fig. 18. (Color online) PMLSM structure diagram.

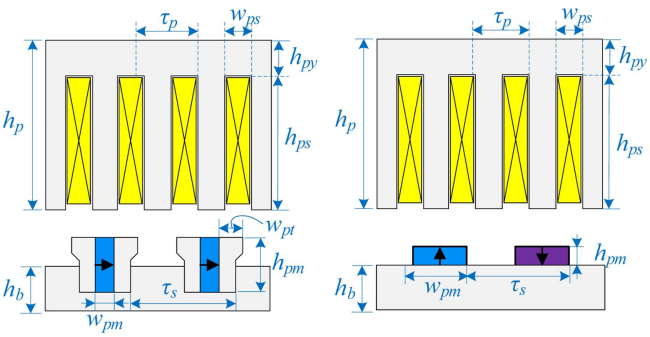

Fig. 19. (Color online) Key parameters of SPMFSLM and PMLSM.

analyzed and compared. The structure diagram is shown in Fig. 19. The key parameters are shown in Table 5. The analysis and comparison principles are as follows:

- The primary structure is the same, only the winding connection mode is different (caused by the special magnetization mode of SPMFSLM).
- Permanent magnet dosage, the same model.
- The same operating conditions (current amplitude, operating speed, etc.).

Fig. 20 is the magnetic density distribution cloud map of PMLSM. The magnetic flux density cloud map of SPMFSLM is shown in Fig. 4(b). It can be clearly found that at the bottom of SPMFSLM secondary permanent magnet, as shown in Fig. 4, there is magnetic flux leakage phenomenon. At the same time, the magnetic density distribution of both motors is relatively uniform and there is no local saturation phenomenon.

The comparative analysis results of the no-load back-EMF of the two machines are shown in Fig. 21(a). The amplitude of the no-load back-EMF of SPMFSLM is 27.48 V, and the amplitude of PMLSM is 31.16 V. The amplitude of PMLSM is 13.39 % higher than that of SPMFSLM. This is also due to the existence of permanent magnetic flux leakage at the bottom of SPMFSLM, as shown in Fig. 4(b).

The thrust comparison between SPMFSLM and PMLSM

Table 5. Key parameters of SPMFSLM and PMLSM.

Items	SPMFSLM	PMLSM
Primary pole pitch, τ_p (mm)	15	15
Primary slot width, w_{ps} (mm)	7.8	7.8
Primary slot height, h_{ps} (mm)	41	41
Primary yoke height, h_{py} (mm)	9	9
Primary height, h_p (mm)	50	50
Primary length (mm)	180	180
Air gap, g (mm)	2	2
Number of turns per coil, N_{coil}	145	145
Copper filling factor	45	45
PM width w_{pm} (mm)	5.4	4.7
PM height h_{pm} (mm)	17.2	17.3
PM dosage (cm^3)	48.76	48.76
Secondary pole pitch τ_s (mm)	25.71	22.5
Backplane height h_b (mm)	10.1	14
Iron material	DW470-50A	DW470-50A
Backplane material	Aluminium	A3 Steel
PM type	N48H	N48H
Rated speed, v (m/s)	1	1
Stack length (mm)	75	75

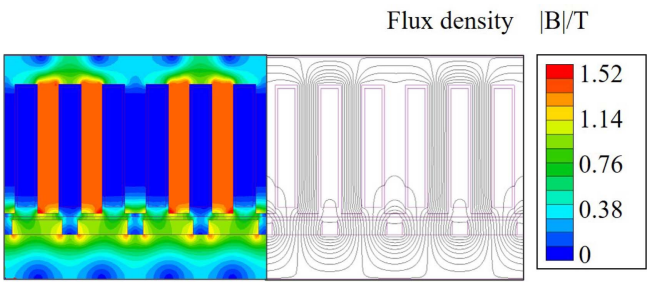

Fig. 20. (Color online) Open-circuit flux density distribution of PMLSM.

is shown in Fig. 21(b). The average thrust of SPMFSLM is 414.2 N, and the average thrust of traditional PMLSM is 456.71 N. The average thrust of PMLSM is 10.26 % higher than that of SPMFSLM. The reason why the average thrust of the traditional PMLSM is higher is shown in Fig. 4(b). Because there is a certain degree of magnetic flux leakage at the bottom of the SPMFSLM secondary permanent magnet, its thrust performance is affected. The thrust fluctuation of SPMFSLM is 2.17 %, and the thrust fluctuation of PMLSM is 4.3 %, which is 98.15 % higher than that of SPMFSLM.

Based on the above considerations, a double-sided SPMFSLM (DS-SPMFSLM) with secondary permanent magnet structure is proposed, which can effectively solve the magnetic flux leakage problem in the single-sided

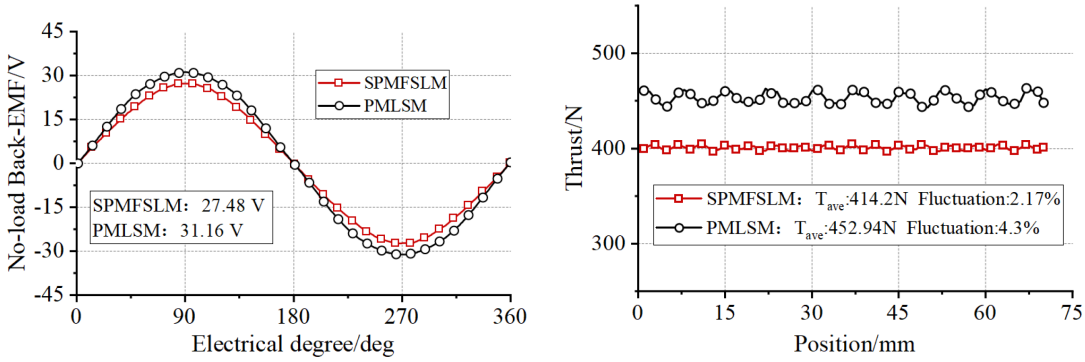

(a) No-load back-EMF (b) Thrust characteristics

Fig. 21. (Color online) Comparison of no-load back-EMF and thrust between SPMFSLM and PMLSM.

SPMFSLM design scheme. The schematic diagram of the double-sided SPMFSLM structure is shown in Fig. 22. It is developed from the single-sided SPMFSLM structure. The primary parts on both sides are mover and can be operated with load respectively. The secondary part containing the permanent magnet in the middle is used as the stator. By adding a mover, and the amount of permanent magnet is unchanged, the mechanical thrust is greatly increased at a small cost, and the mechanical load capacity is significantly improved.

For the DS-SPMFSLM scheme, the same concentrated winding is also used, using a special armature winding connection, as shown in Fig. 22. The part containing the permanent magnet in the middle is an integrated structure, which can be filled with resin material. The magnetization direction of the permanent magnet is consistent, and the

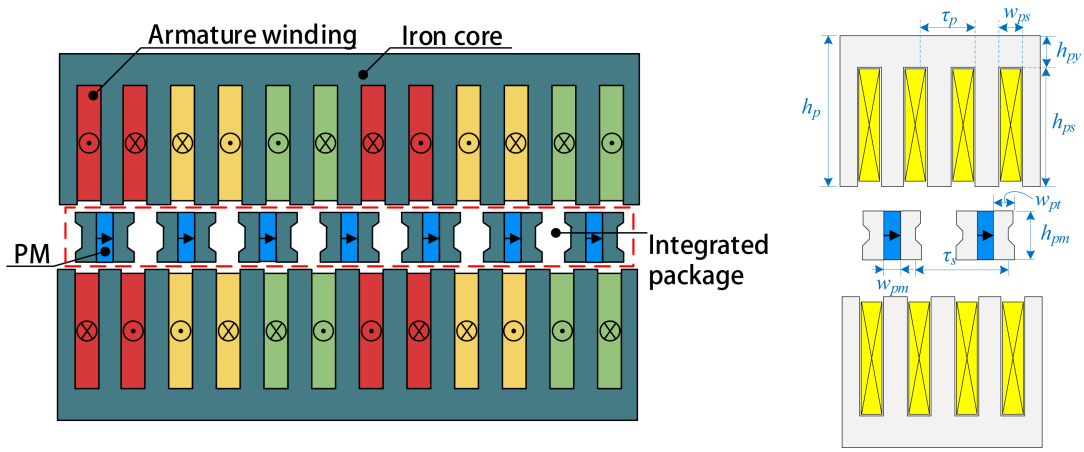

Fig. 22. (Color online) Structure diagram of DS-SPMFSLM.

Table 6. Key structural parameters of DS-SPMFSLM.

Items	DS-SPMFSLM	Items	DS-SPMFSLM
Primary pole pitch, τ_p (mm)	15	PM width w_{pm} (mm)	5.4
Primary slot width, w_{ps} (mm)	7.8	PM height h_{pm} (mm)	17.2
Primary slot height, h_{ps} (mm)	41	PM dosage (cm^3)	48.76
Primary yoke height, h_{py} (mm)	9	Secondary pole pitch τ_s (mm)	25.71
Primary height, h_p (mm)	50	Iron material	DW470-50A
Primary length (mm)	180	Secondary length (mm)	180
Air gap, g (mm)	2	PM type	N48H
Number of turns per coil, N_{coil}	145	Rated speed, v (m/s)	1
Copper filling factor	45	Stack length (mm)	75

operation principle is the same as that of the single-sided SPMFSLM, which follows the principle of the shortest reluctance path.

The parameters of the DS-SPMFSLM simulation model are shown in Table 6. The amount of permanent magnet is consistent with that of SPMFSLM. The materials of each part of the machine, such as iron core, coil and permanent magnet, are the same, and the mechanical operating conditions are the same as those of SPMFSLM.

The no-load magnetic density cloud diagram of DS-SPMFSLM is shown in Fig. 23. The highest magnetic density peak is 1.21 T, and the overall distribution is relatively uniform. It can be clearly found that by adopting a two-sided structure, as shown in Fig. 23 where the red circle is marked, there is no magnetic flux leakage problem, which means that the unit permanent magnet utilization rate is higher, and the mechanical properties can be greatly improved.

The mechanical no-load characteristics of DS-SPMFSLM are shown in Fig. 24(a). The back-EMF amplitude of DS-SPMFSLM is 46.31 V, and the harmonic content of back-EMF is 3.55 %, which is 2.76 % higher than that of unilateral SPMFSLM. By adopting the DS-SPMFSLM structure scheme, the permanent magnet consumption remains unchanged, that is, under the condition of constant permanent magnet cost, higher back-EMF amplitude can be obtained by adding a mover, which means that the performance of the machine will also be greatly improved.

Fig. 24(b) shows the load characteristics of DS-SPMSFSLM. The average thrust of SPMFSLM with bilateral structure is 660.47 N, which is 59.46 % higher than that of SPMFSLM with unilateral structure (414.2 N). The thrust fluctuation of DS-SPMFSLM is 2.18 %, which is almost the same as that of single-sided SPMFSLM (2.17 %). The utilization rate of permanent magnet per unit volume is increased from 8.5 N/cm^3 of SPMFSLM to 13.55 N/cm^3 of DS-SPMFSLM, which is increased by 59.41 %. It can be seen that the utilization rate of permanent magnet is greatly improved after adopting DS-SPMFSLM scheme, and the advantages are obvious.

Based on the above analysis facts, it is obvious that after the unilateral scheme is improved to the bilateral scheme, as shown in Fig. 25, the permanent magnet cost remains unchanged, and only one mover is added on the basis of the unilateral SPMFSLM. At the cost of increasing a small cost, the utilization rate of the permanent magnet per unit volume is improved, and the thrust is greatly

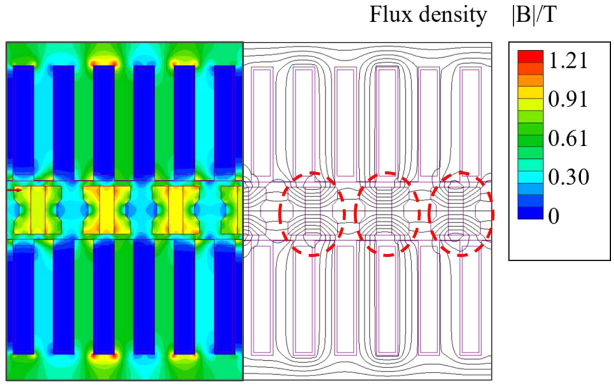

Fig. 23. (Color online) DS-SPMSFLM no-load flux density cloud map.

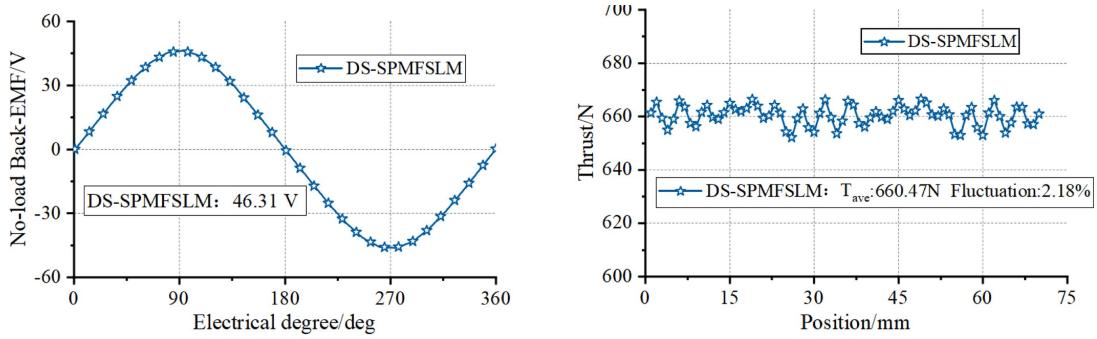

(a) No-load back-EMF (b) Thrust characteristics

Fig. 24. (Color online) No-load back-EMF and thrust characteristics of DS-SPMFSLM.

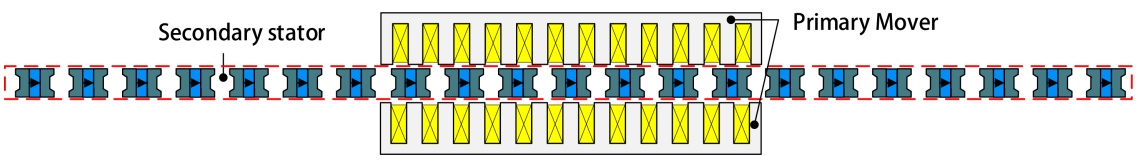

Fig. 25. (Color online) DS-SPMFSLM schematic diagram.

improved. At the same time, the bilateral SPMFSLM can achieve two-way movement, wider application range and higher transportation efficiency. At the same time, higher thrust means that it can withstand greater load and higher power density, especially suitable for long-stroke working fields. At the same time, the mover on both sides can further realize two-way independent operation, which greatly improves the operating efficiency of the motor and expands the application field of machine.

6. Conclusion

In this paper, a SPMFSLM with high thrust density and small thrust fluctuation is proposed. The primary structure strength is greatly improved and the operation is more stable. Based on the analysis of the principle of air gap magnetic field modulation, the multi-objective optimization of the key mechanical parameters is carried out by combining RSM with NSGAII algorithm. Through the comparison of 3D and 2D simulation analysis, the effectiveness of the proposed scheme is cross-validated. At the same time, from the practical point of view, a DS-SPMFSLM is proposed. The relevant conclusions are as follows:

(1) The new topology can provide more space for the winding and permanent magnet, which solves the saturation problem and improves the fault tolerance. Compared with the traditional PPMFSLM, the permanent magnet consumption is only 44.26 %, the cost is greatly reduced, the thrust is increased by 13.7 %, and the thrust fluctuation is reduced from 7.88 % to 2.17 %.

(2) Based on the combination of RSM and NSGAII algorithm, the mechanical structure parameters are optimized, and the optimal parameter combination is selected. The optimized mechanical thrust is increased by 3.34 %, the thrust fluctuation is reduced by 1.84 %, and the harmonic distortion rate of the back EMF is reduced by 9.42 %. The effect is remarkable.

(3) The 3D and 2D simulation results of SPMFSLM show that the difference between the no-load back EMF amplitude of the 3D and 2D models is 1.56 %, the average thrust difference is 1.57 %, and the thrust fluctuation difference is 1.57 %. These results are relatively close, and it can be seen that the 2D and 3D simulations are mutually verified.

(4) By comparing the no-load and load performance of SPMFSLM and PMLSM, based on the characteristics of SPMFSLM, an improved DS-SPMFSLM suitable for long-stroke field is proposed. The permanent magnet cost is unchanged, and only one mover is added at a very low cost, which can greatly increase the thrust.

Acknowledgments

This research was funded by the Foundation of the National Natural Science Foundation of China grant NO. 52177039; The Key Technologies R&D Program of Henan Province of China (NO. 222102220016, 212102210145 and NO. 222102210274).

References

[1] K. Sato, IEEE Trans. Magn. **48**, 4866 (2012).
[2] S. E. Abdollahi and S. Vaez-Zadeh, IEEE Trans. Magn. **50**, 8200809 (2014).
[3] M. Mirzaei, S. E. Abdollahi, and H. Lesani, IEEE Trans. Plasma Sci. **39**, 1566 (2011).
[4] Z. Q. Zhu, X. Chen, J. T. Chen, D. Howe, and J. S. Dai, ICEMS 2948 (2008).
[5] B. Zhang, M. Cheng, R. Cao, Y. Du, and G. Zhang, IEEE Trans. Magn. **50**, 8103004 (2014).
[6] C. F. Wang, J. X. Shen, L. K. Wang, and K. Wang, PEMD 116 (2008).
[7] J. Cai, Q. Lu, Y. Jin, C. Chen, and Y. Ye, ICEMS 1 (2011).
[8] R. Cao, D. Shen, and W. Hua, IEEE Trans. Energy Convers. **36**, 2998 (2021).
[9] R. Cao, M. Cheng, C. Mi, W. Hua, X. Wang, and W. Zhao, IEEE Trans. Energy Convers. **27**, 489 (2012).
[10] D. J. Evans and Z. Q. Zhu, IEEE Trans. Magn. **51**, 1 (2015).
[11] W. Zhao, A. Ma, J. Ji, X. Chen, and T. Yao, IEEE Trans. Ind. Electron. **67**, 80 (2020).
[12] A. Gandhi and L. Parsa, IECON. 2067 (2012).
[13] D. C. J. Krop, L. Encica, and E. A. Lomonova, ICEM. 1 (2010).
[14] Q. Lu, H. Li, X. Huang, D. Ye, Y. Fang, and Y. Ye, ICEM. 237 (2015).
[15] Q. Lu, Y. Yao, J. Shi, Y. Shen, X. Huang, and Y. Fang, IEEE Trans. Ind. Appl. **53**, 4590 (2017).
[16] Q. Lu, H. Li, X. Huang, and Y. Ye, Elect. Electron. Eng. **35**, 832 (2016).
[17] Y. Shen, Q. Lu, H. Li, J. Cai, X. Huang, and Y. Fang, IEEE Trans. Ind. Electron. **65**, 1837 (2018).
[18] A. Gandhi and L. Parsa, IEEE Trans. Magn. **49**, 1436 (2013).
[19] C. T. Liu, C. C. Hwang, P. L. Li, S. S. Hung, and P. Wendling, IEEE Trans. Magn. **50**, 8102704 (2014).
[20] C. Ma and L. Qu, IEEE Trans. Energy Convers. **30**, 1144 (2015).
[21] L. Alberti and N. Bianchi, IEEE-ECCE 3112 (2011).